ADVANCED FUNCTIONAL MATERIALS
www.afm-journal.de

Engineered Interface and Spatial Arrangement of Inorganic Components for Dendrite-Free Li Anodes in Carbonate-Based Electrolyte

Qiannan Zhao, Kaiqi Zhao, Jae-Hoon Baek, Ronghua Wang, Chaohe Xu,* and Jong-Beom Baek**

The practical application of lithium metal batteries (LMBs) in carbonate-based electrolytes is hindered by uncontrolled lithium (Li) deposition behavior. Here, a calcium fluoride (CaF_2) functionalized polyethylene (PE) separator (CF-PE) is developed to spatially rearrange the inorganic components at the Li anode interface. A spontaneous cation exchange reaction between CaF_2 and detrimental lithium carbonate (Li_2CO_3) generates a high modulus lithium fluoride (LiF) layer on the surface of the CF-PE separator with a robust calcium carbonate ($CaCO_3$) enriched solid electrolyte interphase (SEI), enabling dense Li deposition behavior. As a result, the CF-PE separator enabled an extended Li deposition lifespan of more than 1100 h at 1 mAh cm^{-2} and 650 h at 3 mAh cm^{-2}. In Li||NMC622 full cells, the CF-PE separator enabled stable operation over 850 cycles with a low capacity decay rate of 0.025% per cycle. Additionally, the separator retained its structural integrity at 150 °C, with stable cycling of the full cell at 80 °C, greatly outperforming a commercial PE separator. This work presents a practical strategy for constructing dendrite-free LMBs using carbonate-based electrolytes with enhanced electrochemical and environmental tolerance.

1. Introduction

The successful commercialization of lithium-ion batteries (LIBs) has revolutionized environmental policy, the worldwide economy, and modern lifestyles, driving rapid development and the transition toward renewable energy. As demand for energy storage systems increases, next-generation batteries are needed, with higher energy density, prolonged cycling lifespan, broad operating conditions, and enhanced safety. However, when current commercial LIBs are paired with transition metal oxide cathodes and graphite anodes, their energy density is limited to ≈800 Wh L^{-1}.[1] Forming lithium metal batteries (LMBs) by replacing the graphite anode with a Li metal anode is a promising way to overcome the energy density limit of the cells, which also have an intrinsic high theoretical capacity (3860 mAh g^{-1}), low electrochemical potential (−3.04 V vs standard hydrogen electrode), and light weight. However, the practical application of the Li metal anode is limited because of its unstable deposition behavior and associated safety concerns.[2]

The electrochemical performance of Li metal anodes is strongly influenced by the physicochemical characteristics of the electrode–electrolyte interface. The extremely high chemical reactivity of Li causes it to readily react with liquid organic electrolytes upon contact, forming a complex solid electrolyte interphase (SEI).[3] A conventional SEI lacks sufficient mechanical robustness and is unable to endure the stress of repeated Li plating and stripping, which inevitably leads to its degradation and the continuous exposure of fresh Li metal.[4] The continuous growth of the SEI consumes both electrolyte and active Li, thereby accelerating capacity degradation. Furthermore, under repeated cycling stress, the fragile SEI may delaminate from the bulk Li, resulting in the formation of electrically isolated "dead Li."[5] These detrimental processes lead to reduced Coulombic efficiency, elevated internal resistance, and accelerated capacity degradation during cycling. In addition, dendritic Li protrusions can breach the separator, potentially causing internal short circuits and initiating thermal runaway, which poses serious safety risks such as fire or explosion.[6]

The selection of electrolyte solvents and Li salts has a pivotal role in shaping the composition and properties of the SEI on the Li anode. Ether-based electrolytes, for instance, have gained considerable attention due to their ability to promote more stable SEI formation when paired with suitable additives.[7] As a

Q. Zhao, K. Zhao, J.-H. Baek, J.-B. Baek
Department of Energy and Chemical Engineering
Center for Dimension-Controllable Organic Frameworks
Ulsan National Institute of Science and Technology (UNIST)
Ulsan 44919, South Korea
E-mail: jbbaek@unist.ac.kr
Q. Zhao, K. Zhao, R. Wang, C. Xu
National Engineering Research Center for Magnesium Alloys
Chongqing University
Chongqing 400044, P. R. China
E-mail: wangrh@cqu.edu.cn; xche@cqu.edu.cn
The ORCID identification number(s) for the author(s) of this article can be found under https://doi.org/10.1002/adfm.202514348

DOI: 10.1002/adfm.202514348

result, numerous studies have employed Li symmetric cells in ether-based electrolytes, achieving stable cycling over thousands of cycles.[8] However, the limited oxidative stability of ether solvents (<4 V) restricts their use in high-energy-density LMBs. In contrast, carbonate-based electrolytes exhibit superior oxidative stability (up to 6.0 V), making them more suitable for developing high-voltage LMBs.[9]

Upon contact with Li metal, carbonate solvents generate Li alkyl carbonate species that further decompose in the presence of heat, trace water, and certain Li salts, forming lithium carbonate (Li_2CO_3), lithium oxide (Li_2O), and oligoethylene oxides.[10] Among these components, Li_2CO_3 is particularly unstable and prone to continuous degradation. This sequence of decomposition reactions yields a structurally loose and porous SEI, which will further accelerate parasitic side reactions and promote Li dendrite growth, especially undermining long-term cycling stability of the Li metal anode.[11] To address this, incorporating additional inorganic species has been explored to reinforce SEI stability. Notably, constructing a lithium fluoride (LiF)-rich SEI has proven effective at mitigating side reactions and suppressing dendrite formation by increasing the interphase modulus.[12] Fluorinated additives such as vinylene carbonate (VC) and fluoroethylene carbonate (FEC) in the liquid electrolyte have been widely used in carbonate-based systems to enrich LiF content within the SEI.[13] Nonetheless, these strategies depend on the ongoing consumption of expensive fluorinated additives, raising concerns about their sustainability for long-term operation.

Here, we propose a spatial rearrangement of inorganic components at the Li metal anode interface to effectively suppress dendrite growth and enhance the safety of the Li metal anode in carbonate-based electrolytes. We introduced a sacrificial calcium fluoride (CaF_2) layer on the polyethylene (PE) separator (7 µm) and formed a thin composite separator (CF-PE) with a total thickness of 10 µm. The functional LiF and $CaCO_3$ were formed on the surface of the separator and within the SEI, respectively, by successfully displacing the detrimental Li_2CO_3 during cycling. This high modulus interfacial design promoted epitaxial Li growth, rather than dendritic or mossy deposition behavior.

As a result, this strategy enabled the stable cycling of Li metal anodes in carbonate electrolytes for over 1100 h at 1 mA cm^{-2} and 1 mAh cm^{-2}. Even under the high current density and deposition capacity of 3 mA cm^{-2} and 3 mAh cm^{-2}, the Li anode maintained stable cycling performance for more than 650 h, surpassing existing approaches in carbonate systems. Furthermore, the NMC622||Li full cells with this composite separator exhibited over 850 stable cycles with a capacity decay rate as low as 0.025% per cycle. The rational regulation of inorganic interfacial components also markedly enhanced the thermal stability of the separator, supporting reliable battery operation even at elevated temperatures of 80 °C. This work presents a novel interfacial engineering strategy for stabilizing Li metal anodes in carbonate-based electrolytes, offering valuable insights for the development of next-generation high-energy, high-voltage LMBs.

2. Results and Discussion

The accumulation of unstable Li_2CO_3 within the SEI severely deteriorates electrochemical performance. In contrast, LiF is highly valued for its high mechanical modulus and interfacial energy, which makes it a favorable component at the Li anode interface.[14] Accordingly, the following spontaneous ion exchange reaction $Li_2CO_3 + CaF_2 \rightarrow 2LiF + CaCO_3$ with a Gibbs free energy of −15 kJ mol^{-1} can be exploited for interface engineering design. As schematically illustrated in **Figure 1**, CaF_2 is capable of reacting with Li_2CO_3 at the Li anode and electrolyte interface in carbonate-based systems. This type of interface engineering fosters a more uniform ion distribution at the Li surface, facilitating the epitaxial growth of Li with a compact, spherical morphology rather than uncontrolled mossy structures. These densely packed spherical Li deposits can maintain intimate contact with the bulk Li, thereby enhancing structural stability throughout the plating and stripping processes. Additionally, the robust SEI and mechanically resilient interface help buffer volume changes and mitigate mechanical stress during cycling, ultimately preserving the interfacial integrity and suppressing dead Li formation.

We employed CaF_2 as a fluorine source to regulate the interface reaction of the metal Li anode. The CaF_2 nanoparticles with a uniform diameter of 300 nm were prepared by a simple solvothermal reaction (Figure S1, Supporting Information). The X-ray diffraction (XRD) profile of the prepared CaF_2 aligned well with the standard JCPDS card of No. 35–0816 (Figure 1b), confirming the successful preparation of cubic phase CaF_2. From the perspective of optimizing battery architecture, surface modification of the separator offers a straightforward yet effective approach to tailoring the interfacial structure, composition, and mechanical robustness of the Li metal anode. To this end, the as-prepared CaF_2 nanoparticles were directly cast onto a commercial polyethylene (PE) separator, forming a CaF_2-PE composite separator (CF-PE). As shown in Figure S2 (Supporting Information), a large-area fabrication of composite separators could be readily achieved using a simple casting method. A cross-sectional scanning electron microscope (SEM) image of the CF-PE separator exhibited a uniform CaF_2 layer coating with a total thickness of ≈10 µm. Surface SEM analysis of the CF-PE separator in Figure 1d revealed the homogeneous distribution of CaF_2 nanoparticles inside the coating layer. The electrolyte wettability of pristine PE and CF-PE separators was compared. As shown in Figure S3 (Supporting Information), the CF-PE separator exhibited a contact angle of 30°, which is much smaller than the pristine PE separator (39°) with the carbonated electrolyte. In addition, the porosity of CF-PE composite separator was 34.3%, which was comparable to the pristine PE separator (37.4%) and many other modified separators reported in the literature.[15] The enhanced electrolyte infiltration and improved wettability enabled by the CF-functional layer can promote more efficient ion transport and improve the overall mass transfer process in the cell assembly.

The Li deposition performances and behavior in the carbonate electrolyte were investigated by testing Li||Li symmetric cells using CF-PE separator and a pristine PE separator, respectively. As shown in **Figure 2**a, the cell employing the unmodified PE separator exhibited increasing and fluctuating overpotentials during cycling, ultimately experiencing a sharp voltage drop after ≈220 h, indicating cell failure. The symmetric cell with the CF-PE separator retained a stable overpotential throughout the test and achieved a prolonged cycling lifespan exceeding 1100 h (550 cycles), which is over 5 times longer than that of the cell with the pristine PE separator. Even at 3 mA cm^{-2} and 3 mAh cm^{-2}, the

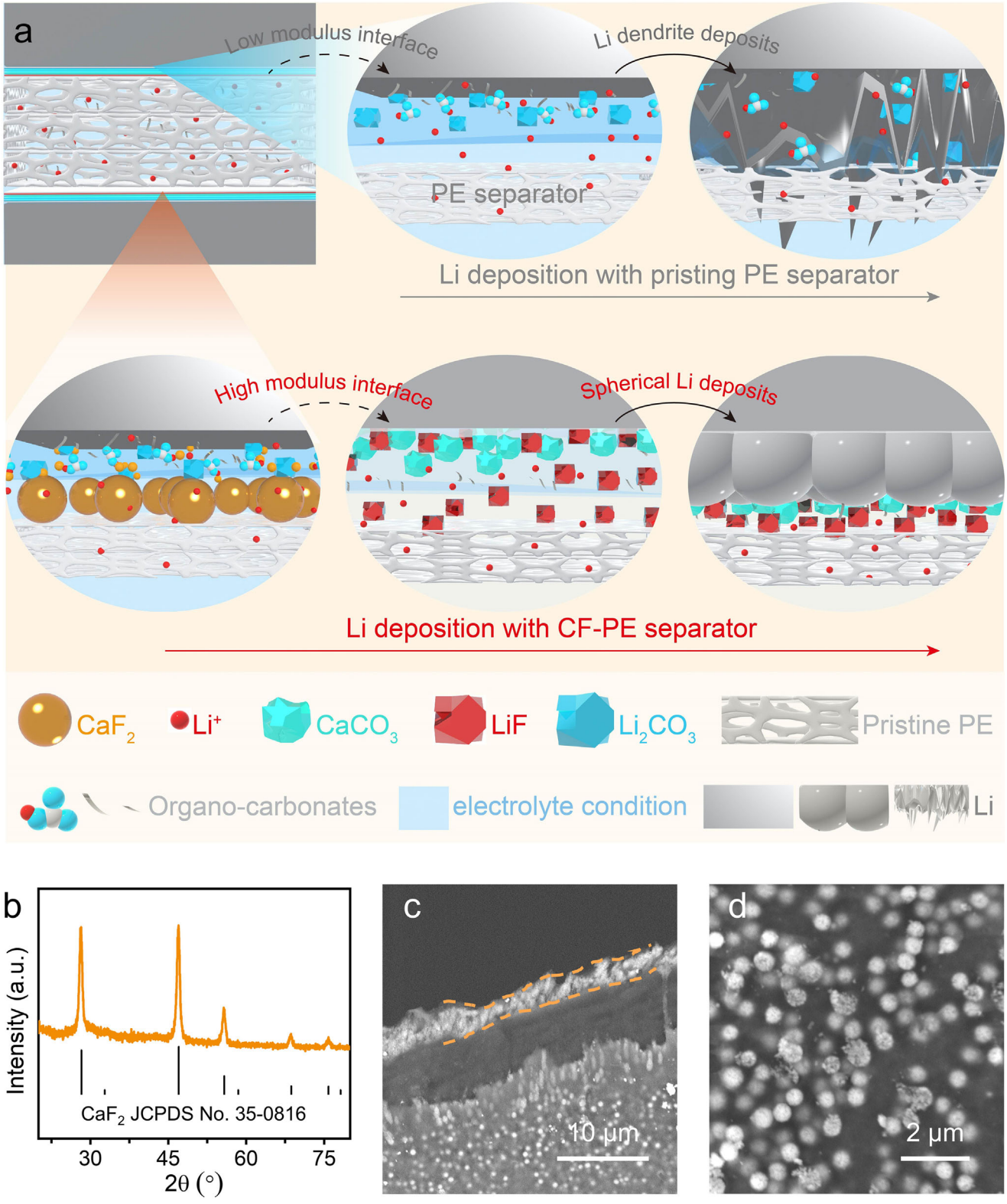

Figure 1. Schematic illustration of Li deposition behaviors and characterization of the CF-PE separator. a) Schematic illustration of Li deposition behavior regulated by the original PE (the top row) and CF-PE separator (the bottom row). b) XRD profile of the synthesized CF_2. c) cross-sectional and d) surface SEM images of the CF-PE separator.

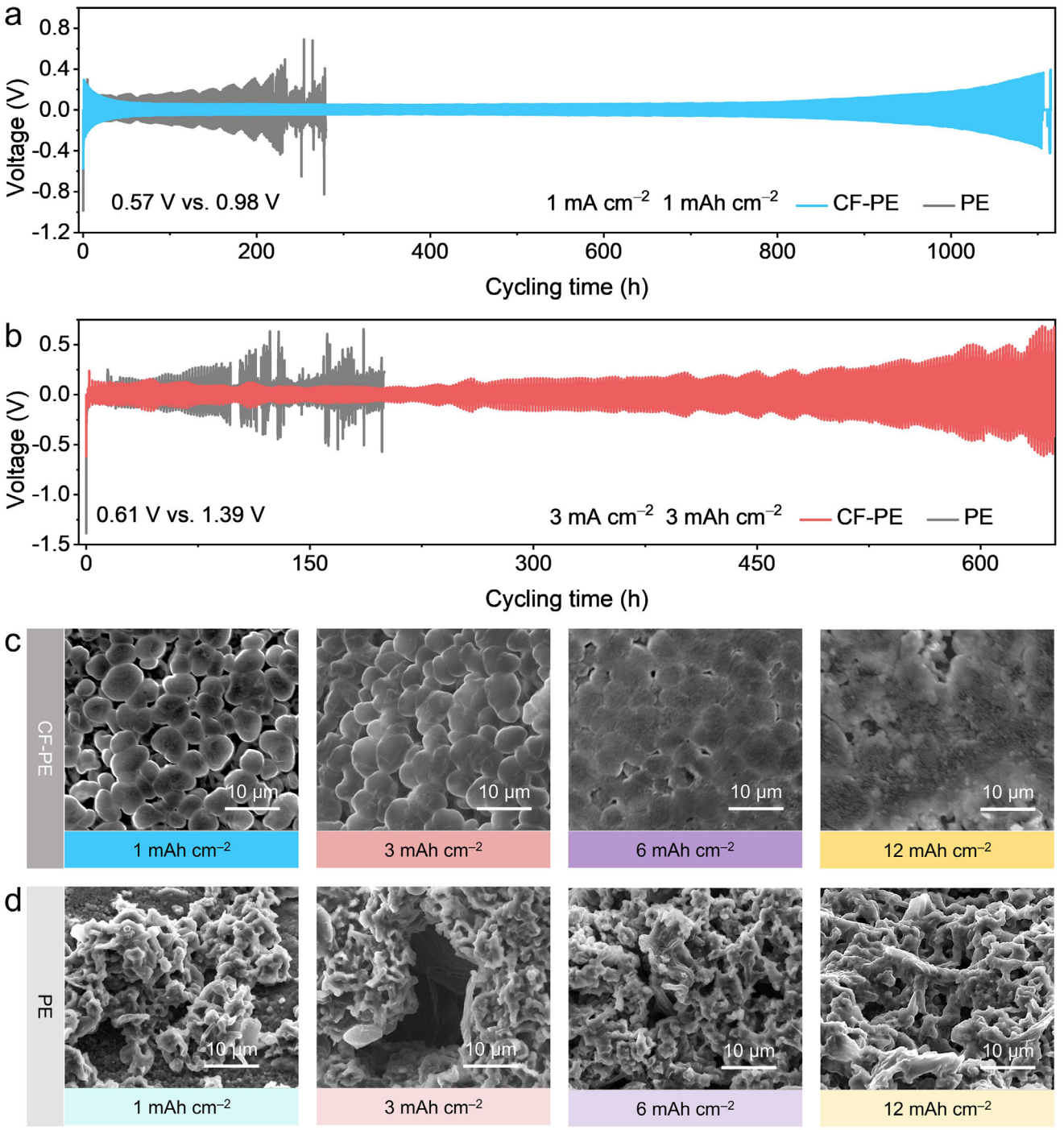

Figure 2. Electrochemical performances and Li deposition behavior characterization of Li metal anodes with different separators. Comparison of the cycling performances of symmetric Li||Li cells regulated by original PE and CF-PE separators at a) 1 mA cm^{-2} and 1 mAh cm^{-2}, b) 3 mA cm^{-2} and 3 mAh cm^{-2}. SEM images of the Li deposition morphologies with area capacities of 1, 3, 6, and 12 mAh cm^{-2} regulated by the c) CF-PE separator and d) original PE separator.

CF-PE-based cell demonstrated stable cycling for 650 h, whereas the cell with the pristine PE separator failed after just 102 h (Figure 2b). Furthermore, the application of the CF-PE separator significantly reduced the initial Li deposition overpotential from 0.98 to 0.57 V at 1 mAh cm^{-2}, and from 1.39 to 0.61 V at 3 mAh cm^{-2}. To exclude the stabilizing contribution from the PVDF binder in the CF-functional layer in the composite separator, the Li||Li symmetric cell using PE separators coated only with PVDF binder (PVDF-PE) was then assembled and tested. As shown in Figure S4 (Supporting Information), the PVDF-PE

was unable to stabilize repeated lithium depositing and stripping reaction, which exhibited pronounced voltage fluctuations after just 132 h (66 cycles). Afterward, the lithium plating/stripping process progressively deteriorated, ultimately leading to cell failure. This result confirmed the critical role of the CaF_2 in the CF-layer to stabilize the electrochemical performance of lithium metal anodes.

The Li nucleation and growth process was confirmed by ex situ SEM characterizations. As shown in Figures 2c and S5 (Supporting Information), the CF-PE separator regulated deposits of micro-sized spherical Li with a deposition capacity of 1 mAh cm^{-2}. When the deposition capacity further increased from 3, 6, to 12 mAh cm^{-2}, the spherical deposits gradually coalesced to form a dense and continuous Li deposition. The micro-spherical Li deposits possess a lower surface area-to-volume ratio, which effectively mitigates electrolyte depletion and minimizes side reactions during repeated plating and stripping. This structural advantage contributes to a lower deposition overpotential and significantly improves the cycling stability of the Li metal anode. In contrast, the Li deposits within a symmetric PE separator-based Li cell exhibited non-uniform Li deposition, and loosely distributed, mossy Li structures with apparent branching were observed even at a low deposition capacity of 1 mAh cm^{-2} (Figure S6, Supporting Information). As the deposition capacity increased, the Li dendrites became significantly thicker, forming highly porous and unstable deposits.

Postmortem analysis was then conducted to evaluate the long-term failure mechanism of the Li||Li symmetric cell with a CF-PE composite separator after cycling over 1100 h (**Figure 2a**). As shown in Figure S7 (Supporting Information), a sudden voltage drop during the delithiation process after 1100 h cycling indicated the onset of an internal micro-short circuit. During the subsequent plating process (at 1110 h, labeled as point 1), the cell temporarily resumed normal operation, suggesting partial reversibility of a short time. A second voltage collapse during the following delithiation confirmed the recurrence of shorting (labeled as point 2). Disassembly of this cell allowed detailed SEM analysis of both lithium electrodes and the separator. As shown in the insets in Figure S7 (Supporting Information), the inadequate deposition sides at points 1 and 2 all maintained a spherical-like morphology without visible dendrites or mossy lithium, indicating a relatively uniform deposition process even after extended cycling. However, the spheres appeared sparsely distributed, which was likely due to gradual electrolyte depletion over time, reducing local Li^+ availability and suppressing compact growth.

Further SEM inspection of the cycled separator revealed large cracks on the PE base layer (highlighted by the red dashed line in the right inset), suggesting that the cell failure was triggered by mechanical fatigue and fracture of the ultrathin PE matrix under long-term electrochemical and thermal stress. In contrast, the CF functional layer played a key role in stress redistribution and crack suppression, explaining the cell's partial voltage recovery after shorting and its superior overall electrochemical stability. All these phenomena indicate that the CF-PE separator could effectively mitigate catastrophic failure and violent shorting events, as evidenced by the absence of sharp voltage oscillations, even in the presence of structural degradation.

Then the underlying working mechanism of the designed CF-PE separator to promote dendrite-free Li deposition was investigated by verifing the surface and spatial chemical state of the Li anode. As shown in **Figure 3a**, the survey XPS spectrum of the CF-PE separator before cycling exhibited detectable Ca 2p signals. However, after cycling, the Ca 2p signal nearly disappeared, while a pronounced Li 1s peak appeared, accompanied by a significant increase in the intensity of the F 1s signal. The high-resolution Ca 2p spectrum further confirmed the absence of Ca-related species on the surface of a cycled CF-PE separator (Figure 3b). Deconvolution of the F 1s spectrum revealed a Ca—F bond peak at 685 eV before cycling, which shifts to a higher binding energy after cycling, indicating the formation of Li—F bonds (Figure 3c). The high-resolution Li 1s spectrum of the cycled CF-PE separator (Figure 3d) could be primarily deconvoluted into a Li—F bond. The minor contributions of alkyl lithium and Li—O species could be attributed to the decomposition of the carbonate-based electrolyte.

To further confirm the interfacial reaction, an XRD analysis of the cycled Li anode regulated by a CF-PE separator was conducted. As shown in Figure 3e, the cycled Li metal anode exhibits strong diffraction peaks corresponding to metallic Li, along with characteristic peaks of $CaCO_3$ (PDF#72-1652). Notably, no significant oxidation products were detected even after 30 min of air exposure, suggesting that the CF-PE separator enables the formation of a compact and protective interphase on the Li surface, thereby enhancing its air stability.

Time-of-flight secondary ion mass spectrometry (TOF-SIMS) depth profiling results were employed to reveal the spatial distribution of chemical species at the interface between the CF-PE separator and the Li metal anode. As shown in Figure 3f,g, the surface of the cycled CF-PE separator is covered by C–H species along the depth direction. The depth profile of functional CaF_2 exhibits relatively weak signal intensity near the surface, while remaining consistently detectable in the deeper regions. In contrast, the LiF species display a complementary distribution, with a distinct LiF-rich layer located beneath the surface. These observations are in good agreement with the XPS results and further confirm that the LiF formation can be attributed to the interfacial reaction involving the introduced CaF_2. For the cycled Li metal anode regulated by the CF-PE separator, the solid electrolyte interphase (SEI) layer is composed of organic C–H species and uniform distributions of $CaCO_3$ along with a small amount of LiF.

The composition profiles of Li_2CO_3 provided key insights into the interfacial reactions involving the carbonate-based electrolytes. Only trace amounts of Li_2CO_3 were detected on the surface of the CF-PE separator (Figure 3h), and it was nearly absent on the Li metal surface. On the other hand, the SEI layer on the cycled Li metal anode with an original PE separator exhibited a pronounced and continuous distribution of C–H, Li_2O, LiF, and Li_2CO_3 species along the depth direction (Figure 3j–k), indicating severe organic electrolyte decomposition side reactions happened without any regulation.

As shown in Figure S8 (Supporting Information), the cycled lithium surface in the symmetric Li||Li cells with the CF-PE separator exhibited a clear absence of carbonate-related IR absorption peaks (≈740 cm^{-1} and 1350–1450 cm^{-1}), whereas strong carbonate signals are observed on the surface of the cycled CF-PE separator.[16] Combined with XPS and XRD results, this indicated the formation of $CaCO_3$ through ion-exchange reactions in the CF layer. Moreover, the cycled CF-PE separator displayed a

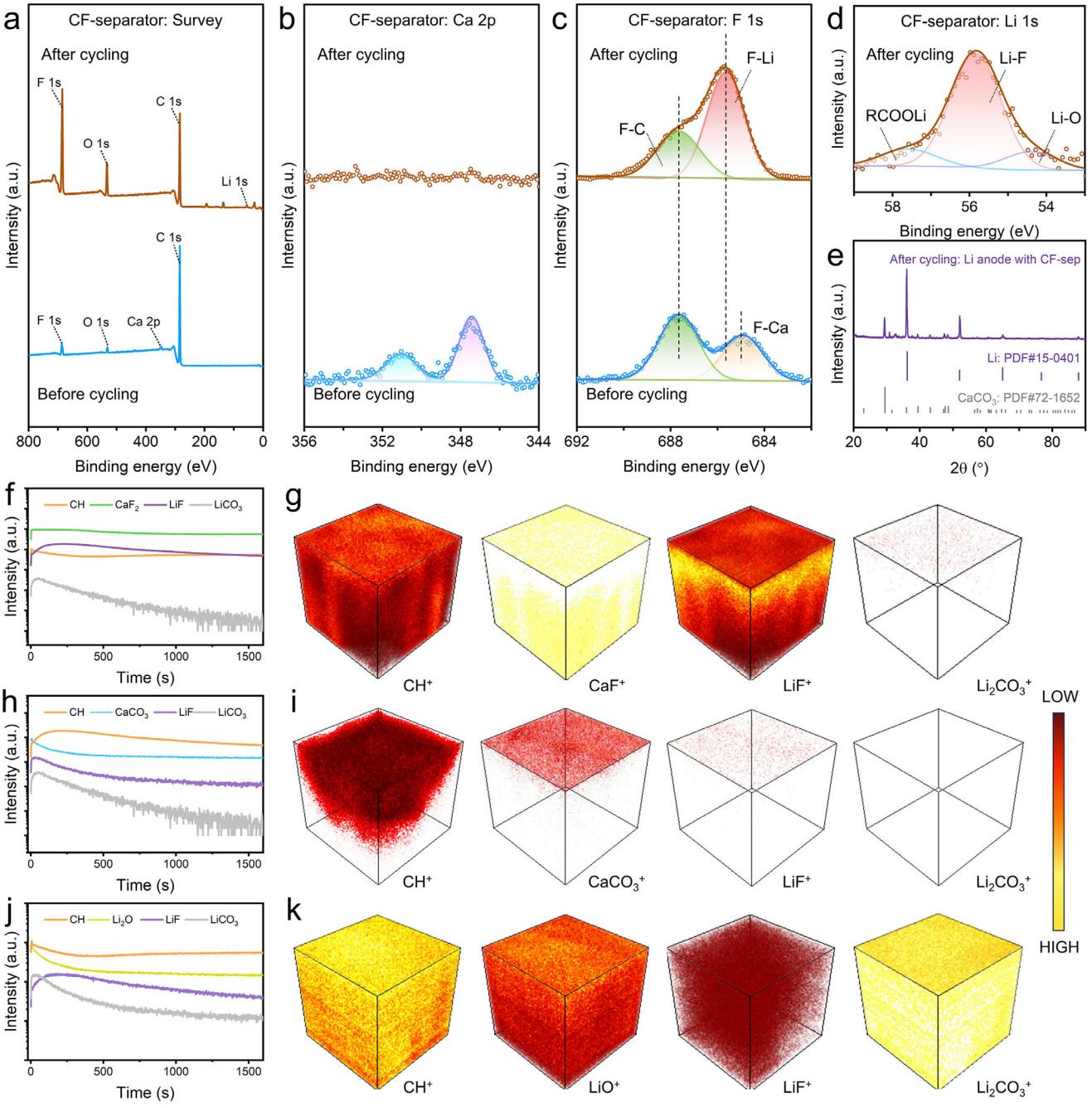

Figure 3. Surface chemical environment investigations of the cycled Li anode and separators. XPS a) survey, b) Ca 2p, c) F 1s, and d) Li 1s spectra of CF-PE separator before and after cycling. e) XRD profile of the cycled Li anode regulated by the CF-PE separator. TOF-SIMs results of f,g) CF-PE separator, h,i) Li anode after cycling with CF-PE separator, and j,k) Li anode after cycling with PE separator. f,h,j) are the depth profilings. g,i,k) 3D reconstricted distribution of CH^+, CaF^+, LiF^+, $Li_2CO_3{}^+$, $CaCO_3{}^+$, LiO^+ of second ion species.

pronounced Li-F typical absorption signal at ≈530 cm^{-1}, further corroborating the interfacial stabilization mechanism.[17] The slight displacement of characteristic peaks could be attributed to the intricate interfacial chemistry taking place at the anode surface, reflecting the dynamic nature of electrode–electrolyte interactions. In sharp contrast, the symmetric Li||Li cell using pristine PE separator showed distinct carbonate signals on both the cycled Li surface and the cycled PE separator, indicative of substantial Li_2CO_3 accumulation from electrolyte decomposition. These results provide compelling evidence that the CF-PE separator promotes interfacial ion-exchange reactions at the lithium surface, leading to a more stable, inorganic-rich interphase.

The well-defined SEI structure and composition on the Li metal anode surface regulated by the CF-PE separator were further characterized using SEM and transmission electron microscopy (TEM), as shown in **Figure** 4a–c. A symmetrical Li

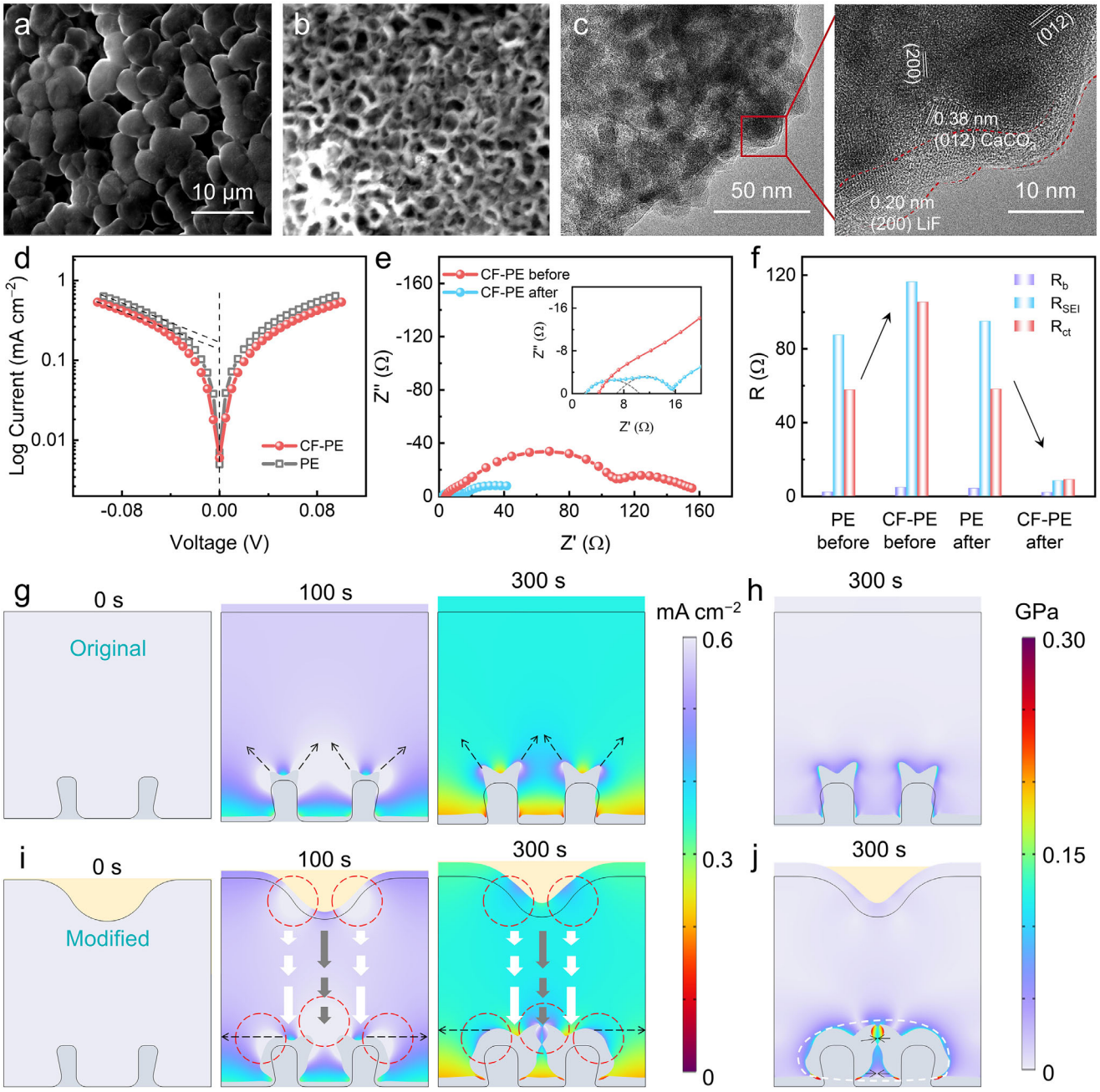

Figure 4. SEI characterization of the symmetric Li||Li cell and theoretical simulation of Li deposition behavior with different interface properties. SEM image of a) the Li deposited terminal and b) Li stripped terminal in the symmetric Li||Li cell regulated by CF-PE separator. c) TEM and high-resolution TEM images of the SEI in the Li metal anode regulated by the CF-PE separator. d) Polarization plots of the symmetric Li||Li cell with PE and CF-PE separator, respectively. e) Nyquist plots of the symmetric Li||Li cell with CF-PE separator before and after cycling. f) Comparison value of the bulk resistance (R_b), SEI resistance (R_{SEI}), and charge transfer resistance (R_{ct}) of the symmetric Li||Li cell with CF-PE separator before and after cycling. Theoretical simulation of Li deposition process regulated by g–j) CF-PE separator and g,h) original PE separator. g,i) The electrolyte current density distributions. h,j) Stress distributions.

metal cell with a CF-PE separator was cycled stably for 100 cycles before disassembling (Figure S4, Supporting Information). At a deposition capacity of 3 mAh cm^{-2}, the Li deposition side exhibited a fused and quasi-spherical morphology (Figure 4a), consistent with previous observations. After full removal of the active Li deposits, the void shell structure was well preserved on the Li striped side (Figure 4b). TEM and high-resolution TEM images further revealed distinct lattice fringes with spacing of 0.2 and 0.38 nm within the SEI, corresponding to the (200) and (012) crystal planes of LiF and $CaCO_3$, respectively.

Based on the above results, the absence of Li_2CO_3 at the Li interface indicated that it was being efficiently consumed

through interfacial reactions within the CF-PE separator system, and the resulting stable interface further inhibited the subsequent side reactions associated with electrolyte decomposition. This confirmed that the ion exchange reaction between CaF_2 and Li_2CO_3 at the interface facilitated the spatial redistribution of inorganic LiF and $CaCO_3$ components at the Li interface. Additionally, the involvement of Li_2CO_3 as a Li source also reduces the demand for additional Li consumption, contributing to improved material utilization and enhanced interfacial stability.

The exchange current densities of symmetric Li||Li cells assembled with different separators were evaluated by fitting the intercepts of Tafel plots. As shown in Figure 4d, the cell using the CF-PE separator exhibits an exchange current density of 1.51 mA cm^{-2}, which is significantly higher than that of the cell with the pristine PE separator. This result indicates that the CF-PE separator effectively enhances the interfacial ion transport kinetics.

Electrochemical impedance spectroscopy (EIS) measurements were performed to evaluate the interfacial charge-transfer behaviors, as shown in Figures 4e and S9–S11 (Supporting Information). The Nyquist plots of both cells display two depressed semicircles in the high and med-high frequency region, corresponding to the SEI resistance (R_{SEI}) and the charge transfer resistance (R_{ct}), respectively. The fitted values of bulk resistance (R_b), R_{SEI}, and R_{ct} are shown and summarized in Figure 4f and Table S2 (Supporting Information). The introduction of the CF functional layer initially increased the value of both R_{SEI} and R_{ct} in the fresh cell, indicating the CaF_2 layer can hardly improve the interfacial reaction kinetics. However, the cycled Li symmetric cell with the CF-PE separator exhibited greatly decreased values of both R_{SEI} and R_{ct}, which were much lower than those observed in the cycled cell with the pristine PE separator. These results demonstrate that the effective redistribution of inorganic components regulated by the CaF_2-PE separator leads to the formation of a stable Li interface with improved ion transport properties. As shown in the previous results, the CF-PE separator maintained high porosity with improved electrolyte wettability and charge-transfer characteristics. Given that identical electrolyte loadings were used in the electrochemical tests, it could be inferred that the CF-PE separator suggested superior rate capability and cycling stability without requiring additional electrolyte loading compared to the pristine PE separator.

To further elucidate the Li deposition mechanism, theoretical models were established comparing Li deposition regulated by the CF-PE separator and the PE separator. Simulations were carried out to investigate the deposition dynamics and interfacial characteristics of Li metal with surface protrusion defects (Figure S12, Supporting Information). The modeling results revealed that Li tends to nucleate and deposit preferentially at microscopic surface protrusions in the above two systems. However, in the case of the PE separator, Li growth predominantly occurred along the longitudinal axis of the protrusions, resulting in the formation of branched structures and an increased aspect ratio of the deposits (Figure S13, Supporting Information). In contrast, the CF-PE separator promotes a higher lateral epitaxial growth rate, leading to the formation of flattened Li deposits with a significantly reduced aspect ratio. As the deposition capacity increases, these lateral structures progressively coalesce into a dense morphology, consistent with the experimental SEM observations.

Next, the electrolyte current density and stress distribution on the Li metal interface during deposition were analyzed. The electrolyte current density indicated a spatially inhomogeneous ion distribution, which tended to concentrate at microscopic Li protrusions. This non-uniformity drives a preferential Li deposition at these regions, leading to dendritic Li growth in the PE separator system, ultimately leading to dendritic growth that evolves into a mossy morphology (Figure 4g). The formation of such localized current hotspots is inherently driven by electric field distortions caused by interfacial defects. In contrast, the CF-PE separator model exhibited a complementary current distribution pattern on the corresponding separator surface, as highlighted by the red dashed circles in Figure 4i. This redistribution of the electrolyte current effectively suppresses longitudinal Li growth and mitigates the tip-amplification effect, thereby promoting uniform deposition in the form of smooth, quasi-spherical Li structures. Additionally, stress distribution analysis indicated that the elongated Li deposits observed in the PE separator model experience more regions with high stress concentration, making them more susceptible to mechanical fracture and pulverization (Figures 4h, 4j; Figure S14, Supporting Information). In comparison, the quasi-spherical Li deposits formed in the CF-PE separator model exhibit less stress concentration, further supporting the enhanced structure of this deposition behavior.

As shown in **Figure 5a**, the CF-PE separator enabled the cationic exchange reaction to happen at the Li anode interface, that is, $Li_2CO_3+CaF_2 \rightarrow 2LiF+CaCO_3$. According to the Gibbs free energy data in Table S3 (Supporting Information), this reaction is thermodynamically spontaneous, with a Gibbs free energy of -15 kJ mol^{-1}. Although this is a solid-state ion exchange reaction, it may be limited by ion diffusion and the reactant contact area, and the presence of an internal electric field inside the battery will facilitate its progression. Driven by the internal electric field, various ions, especially the charge carrier Li ions in LMBs, can freely migrate to the surfaces of solid Li_2CO_3 and CaF_2, thereby ensuring an ion supply at the reaction interface. Moreover, the internal electric field can modulate the surface polarization of solid materials, which in turn influences their ion adsorption and desorption behaviors. All these effects collectively enhance the kinetics of the solid-state ion exchange reaction at the Li metal anode interface, promoting its occurrence and contributing to the formation of a stable and functional interphase.

In summary, the application of the CF-PE separator ensures the ion exchange reaction, resulting in the redistribution of high modulus LiF and $CaCO_3$ at different locations, as schematically illustrated in Figure 5b. Specifically, LiF is produced on the surface of the PE separator, while $CaCO_3$ is incorporated into the robust SEI layer on the Li anode. Compared to the uncontrolled, loose, moss-like dendritic Li deposits typically observed with conventional separators, the high-modulus and high-surface-energy interface constructed by the CF-PE separator effectively suppresses the tip-amplification effect. This promotes the lateral, epitaxial growth of Li into compact, spheroid-like morphologies rather than irregular dendrites.

The resulting dense Li deposits maintain strong interfacial adhesion and a large contact area with the underlying substrate, thereby mitigating volume fluctuation during repeated

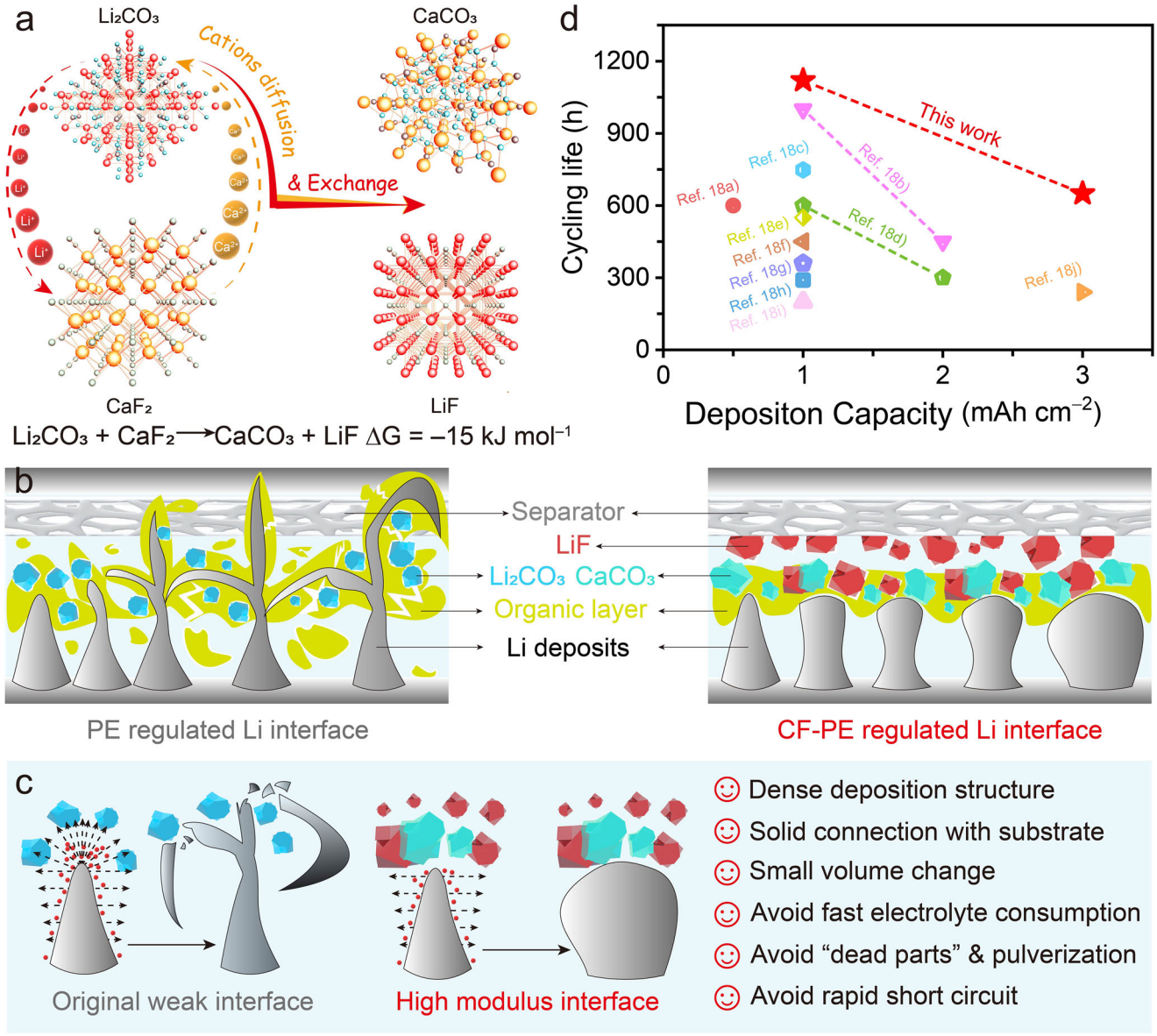

Figure 5. Schematic illustration of the functionality of the CF-PE separator. a) Cationic exchange reaction mechanism at the Li interface regulated by the CF-PE separator. b,c) Schematic illustration of the Li deposition regulation effect produced by the original PE and the designed CF-PE separator. d) Li stabilization capability of the CF-PE separator compared with current advanced strategies[18] for improving the Li cycling performance in carbonated-based electrolyte.

plating/stripping cycles. Furthermore, this compact deposition structure minimizes the direct exposure of metallic Li to the liquid electrolyte, thereby suppressing side reactions inherent to carbonate-based systems. As a result, the formation of dead Li and pulverization is reduced, and the risk of internal short circuits is significantly mitigated. These synergistic effects collectively lead to a substantial extension of the cycling lifespan of Li metal anodes in carbonate electrolytes, outperforming existing strategies aimed at stabilizing Li interfaces in such systems (Figure 5c). The developed CF-PE broke the conventional trade-off by simultaneously enabling high-capacity deposition and long-term stability under harsh conditions in carbonate electrolyte. As shown in Figure 5d and Table S5 (Supporting Information), the CF-PE separator with a thin thickness enabled both extended cycling life and high deposition capacity of the Li anode, significantly outperforming previously reported modification strategies of separators in carbonate-based electrolytes.[18] It is concluded that this strategy introduces a LiF-functional interphase at the interface of the Li metal anode while simultaneously consuming electrochemically harmful Li_2CO_3, without depleting additional Li ions. This interfacial engineering concept offers a versatile route toward the removal and efficient conversion of detrimental Li_2CO_3 at all kinds of interfaces in next-generation energy storage systems.

It has been a concern that the transformation pathway in battery systems often induces large volume changes that threaten

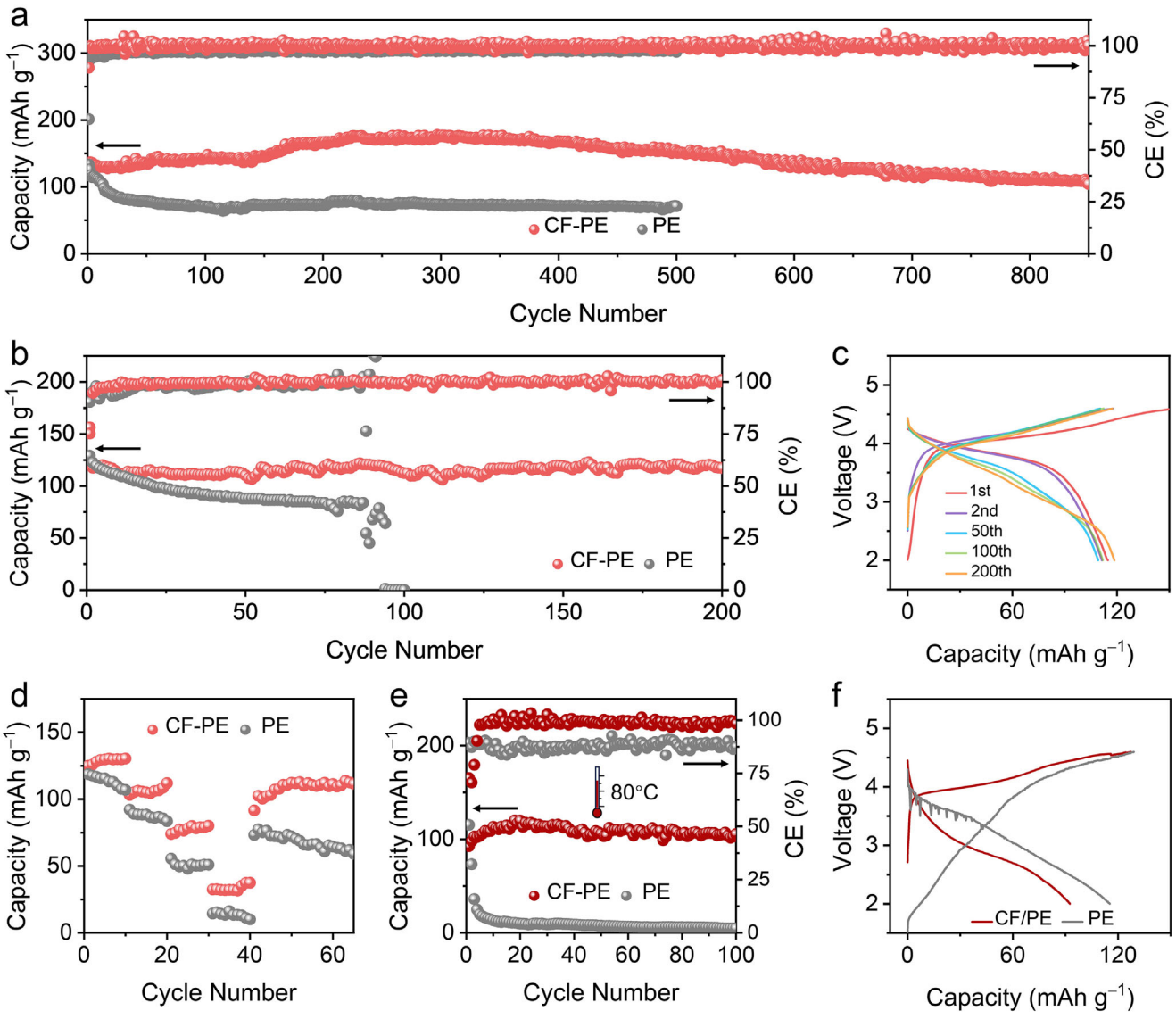

Figure 6. Electrochemical performances of Li||NMC622 full cells with CF-PE separator and PE separator. a) Ultra-long cycling performance at 1C with a cathode loading of 1.2 mg cm^{-2}. b) Comparison of cycling performance at 0.5 C with a cathode loading of 4.1 mg cm^{-2}. c) Voltage profiles during cycling in (c). d) Rate performances. e) Cycling performances at a high temperature of 80 °C. f) Voltage profiles of the first cycle in (d).

interfacial stability, but this work involves a slow interfacial ion-exchange reaction, rather than the bulk conversion between Ca^{2+} from the CF-functional layer and Li^+ from Li_2CO_3 in the native SEI. This transformation proceeds gradually, as reflected by the initially higher overpotential in CF-PE-based Li||Li cells (Figure 2a,b), which decreased and stabilized upon cycling. This result contrasts with the rising polarization and early failure in PE-based cells. The associated volume changes calculated based on the densities of the related materials in Table S4 (Supporting Information) (≈24% expansion in SEI and ≈17% contraction in CF layer) remain below 30%. Further considering the mild ionic exchange reaction kinetics, this reaction will cause minimal structural disruption.

The CF-PE separator was further applied to a Li metal full cell, paired with a Li metal anode and NMC622 cathode to evaluate its practical application potential. As shown in **Figure 6a–c**, the use of the CF-PE separator did not affect the full cell reaction, as the discharge capacity of the LMB with the CF-PE separator was similar to that of the battery with a PE separator in the early cycles. However, the CF-PE separator significantly enhances the cycling stability and Coulombic efficiency of the full cell, while the cell with the PE separator exhibits continuous degradation in discharge capacity. This capacity fading is primarily attributed to unstable Li plating/stripping behavior at the anode interface.

As shown in Figure 6a, the Li metal full cell with a CF-PE separator, with a moderate cathode loading configuration of 1.2 mg cm^{-2} achieved a high initial discharge capacity of 137.7 mAh g^{-1} at 1 C and maintained 78% capacity retention after 850 cycles, corresponding to a low capacity decay rate of 0.025%

per cycle. In contrast, the Li full cell with a PE separator showed a similar initial discharge capacity of 133.6 mAh g^{-1} under the same test conditions, but it suffered a 32.9% capacity loss only within the first 20 cycles.

When the cathode loading was improved to 4.1 mg cm^{-2}, the use of the CF-PE separator ensured full cell stable cycling for 200 cycles (Figure 6c). Although the average discharge voltage exhibited only a slight decline throughout cycling, the discharge capacity remained nearly unchanged. This phenomenon can be attributed to the degradation of the crystal structure of the cathode material, which could be resolved by optimizing the cathode material in the future. Conversely, the Li metal full cell using the PE separator not only suffered from rapid capacity decay but also exhibited noticeable capacity fluctuations and a short-circuit failure after 94 cycles. Additionally, the application of the CF-PE separator also significantly improved the rate performance of the Li metal full cells as shown in Figure 6d.

The thermal safety of Li metal full cells is directly governed by the thermal resistance of the employed separator.[19] High temperature conditions higher than 130 °C were intentionally selected to simulate extreme thermal abuse scenarios, often used in material screening protocols to assess tolerance under the safety-critical condition of the polymer separator. These thermoresistance tests closely relate to realistic thermal abuse scenarios in the full cell, such as overcharge, external short circuits, or internal micro-short circuit.[20] The localized temperatures can briefly exceed 130 °C under such extreme conditions, causing the polymer separator to melt and shrink, amplifying the likelihood of thermal runaway and leading to severe safety concerns.

Benefiting from the incorporation of inorganic components, the CF-PE separator demonstrated superior high-temperature resistance compared to the pristine PE separator. As shown in Figure S15 (Supporting Information), the CF-PE separator maintained its structural integrity at 130 °C with minimal shrinkage, while the pristine PE separator underwent severe shrinkage and visible rupture under the same conditions. Thermal imaging during the heating process revealed a more uniform heat distribution across the CF-PE separator, along with reduced surface thermal scattering. These observations suggest excellent thermal insulation properties are provided by the functional modification layer, as well as enhanced environmental tolerance. When the temperature was further elevated to 150 °C, the PE separator exhibited pronounced shrinkage, thermal fatigue, and extensive crack formation after 6 h of heating. In contrast, the CF-PE separator remained intact, showing no signs of deformation or degradation, thereby significantly improving the thermal safety of LMBs.

To evaluate its practical electrochemical stability under thermal stress, we further tested the cycling performance of Li metal full cells assembled with the CF-PE separator at 80 °C. As shown in Figure 6e, the full cell with the pristine PE separator experienced micro-short circuiting within the first cycle and completely lost capacity in subsequent cycles. In sharp contrast, the cell using the CF-PE separator delivered stable cycling for 100 cycles at 80 °C, clearly demonstrating the importance of thermal stability in maintaining long-term cell performance. The outstanding electrochemical performance of the CF-PE separator under both ambient and elevated temperature conditions highlights its strong potential for practical application in high-performance Li metal full cells. To demonstrate practical applicability, a soft-packaged lithium metal full cell was assembled using the CF-PE composite separator. As shown in Figure S16 (Supporting Information), the charged cell exhibited a stable open-circuit voltage of ≈4.4 V and was able to successfully illuminate a string of multicolor LEDs (Movie S1, Supporting Information), confirming its reliable output capability and potential for real-world applications.

Then, the electrochemical performance of the full cells with a low N/P ratio of 1.5 was further compared with CF-PE and PE separators. The Li@Cu anode with limited Li resource was first prepared in a Cu|Li half-cell by the electrodeposition method. Because the theoretical area capacity of the cathode was ≈0.82 mAh cm^{-2}, the Li deposition current density and area capacity were set as 1.23 mA cm^{-2} and 1.23 mAh cm^{-2}, respectively. As shown in Figure S17a (Supporting Information), the Li deposition profile indicated that the CF-PE separator showed a much lower deposition overpotential of 117 mV than the PE separator (339 mV). This result confirmed the Li deposition-regulating effect of the CF-PE separator. The prepared Li@Cu anodes were then used to assemble Li@Cu||NMC622 full cells using the CF-PE or PE separator. As shown in Figure S17b,c (Supporting Information), the CF-PE separator displayed a high discharge capacity of 126.6 mAh g^{-1} (based on the active cathode material loading) with high stability for 30 cycles. In sharp contrast, the full cell using a conventional PE separator with limited Li supply only delivered a discharge capacity of 65.2 mAh g^{-1}, suffering from rapid capacity decay and declining CEs from the early cycles. These results further confirmed that the CF-PE separator effectively suppressed side reactions and improved the reversibility of the Li anode not only in asymmetric half-cells but also in full cells under limited Li conditions, underscoring its potential for practical applications.

The electrolyte compatibility of the designed CF-PE composite separator was further evaluated using a typical ether-based electrolyte (1 M LiTFSI in DOL/DME with 2% $LiNO_3$). As shown in Figure S18 (Supporting Information), the symmetric Li||Li symmetric cell employing the CF-PE separator exhibited lower deposition overpotentials and maintained stable cycling performance in this electrolyte system. In contrast, Li||Li symmetric cells assembled with pristine PE or PVDF-coated PE separators showed a marked increase in overpotential after only 30 h cycling, indicating fast deteriorating interfacial reactions at the Li surface. These results demonstrated the stabilizing effect of the CF-PE separator on lithium metal anodes across different electrolyte systems, highlighting its broad compatibility and promising application potential.

3. Conclusion

In conclusion, we achieved dendrite-free Li metal deposition in carbonate-based electrolytes by introducing a CaF_2 functional layer onto the separator surface, simultaneously enhancing its electrochemical and environmental tolerance in harsh conditions. A high modulus LiF interfacial layer and $CaCO_3$-enriched SEI were formed at the Li metal anode interface, rather than an unstable Li_2CO_3 interphase, through a cation exchange reaction. This interfacial engineering strategy effectively mitigated tip-induced amplification during Li deposition, suppressed

electrolyte side reactions, and promoted the formation of dense, spheroid-like Li deposits. As a result, the Li metal anode with the CaF_2-PE separator exhibited a stable cycling lifespan of 1000 h at 1 mAh cm^{-2} and 650 h at 3 mAh cm^{-2}, improving its cycling stability by 3–6 times. Benefiting from its stabilizing effect on the Li metal anode, the CaF_2-PE separator enabled Li||NMC622 full cells to achieve stable cycling performances, significantly outperforming those with the pristine PE separator. Additionally, the CaF_2-PE separator ensured the thermal tolerance of the Li metal full cells, maintaining stable cycling at 80 °C, whereas the counterpart with the PE separator failed to operate properly under these conditions. These findings underscore the applicability of this separator engineering approach for stabilizing lithium metal batteries in carbonate-based electrolytes, paving the way toward high-energy systems with reduced lithium excess.

Supporting Information

Supporting Information is available from the Wiley Online Library or from the author.

Acknowledgements

This work was supported from the National Research Foundation of Korea (RS-2023-00221668, RS-2024-00435493, RS-2024-00466616), Natural Science Foundation of Chongqing, China (CSTB2024NSCQ-LZX0013, CSTB2024NSCQ-MSX1062), Chongqing Overseas Chinese Entrepreneurship and Innovation Support Program (No. cx2022002), and Chengdu Regional Science and Technology Innovation Cooperation Project (2023-YF11-00066-HZ).

Author Contributions

Q.Z. conceived the idea. R.W., C.X., and J.-B.B. provided the financial support and supervised this work. Q.Z. and K.Z. helped electrochemical tests and thoretical simulations. Q.Z., K.Z., and J.-h.B. helped with the materials characterization. Q.Z., R.W., C.X., and J.-B.B. prepared the manuscripts.

Conflict of Interest

The authors declare no conflict of interest.

Data Availability Statement

The data that support the findings of this study are available from the corresponding author upon reasonable request.

Keywords

CaF_2/Li_2CO_3/LiF, carbonate electrolyte, ion exchange reaction, lithium metal anode, separator modification

Received: June 8, 2025
Revised: August 19, 2025
Published online:

[1] a) Z. Wu, C. Wang, Z. Hui, H. Liu, S. Wang, S. Yu, X. Xing, J. Holoubek, Q. Miao, H. L. Xin, P. Liu, *Nat. Energy* **2023**, *8*, 226; b) S. Kim, G. Park, S. J. Lee, S. Seo, K. Ryu, C. H. Kim, J. W. Choi, *Adv. Mater.* **2023**, *35*, 2206625.

[2] Y. Jie, S. Wang, S. Weng, Y. Liu, M. Yang, C. Tang, X. Li, Z. Zhang, Y. Zhang, Y. Chen, F. Huang, Y. Xu, W. Li, Y. Guo, Z. He, X. Ren, Y. Lu, K. Yang, S. Cao, H. Lin, R. Cao, P. Yan, T. Cheng, X. Wang, S. Jiao, D. Xu, *Nat. Energy* **2024**, *9*, 987.

[3] D. Luo, L. Zheng, Z. Zhang, M. Li, Z. Chen, R. Cui, Y. Shen, G. Li, R. Feng, S. Zhang, G. Jiang, L. Chen, A. Yu, X. Wang, *Nat. Commun.* **2021**, *12*, 186.

[4] a) X. Zhou, F. Huang, X. Zhang, B. Zhang, Y. Cui, Z. Wang, Q. Yang, Z. Ma, J. Liu, *Angew Chem., Int. Ed.* **2024**, *63*, 202401576; b) J. N. Gongxun Lu, D. Luan, X. Tao, X. Wen, D. Lou, *Sci. Adv.* **2023**, *9*, adf1550.

[5] a) B. Jagger, M. Pasta, *Joule* **2023**, *7*, 2228; b) J. Y. Kim, O. B. Chae, M. Wu, E. Lim, G. Kim, Y. J. Hong, W.-B. Jung, S. Choi, D. Y. Kim, I. Gereige, J. Suk, Y. Kang, H.-T. Jung, *Nano Energy* **2021**, *82*, 105736.

[6] Q. Sun, Z. Cao, Z. Ma, J. Zhang, W. Wahyudi, G. Liu, H. Cheng, T. Cai, E. Xie, L. Cavallo, Q. Li, J. Ming, *Adv. Funct. Mater.* **2022**, *33*, 2210292.

[7] a) S. Stuckenberg, M. M. Bela, C. T. Lechtenfeld, M. Mense, V. Kupers, T. T. K. Ingber, M. Winter, M. C. Stan, *Small* **2024**, *20*, 2305203; b) Q. Zhao, N. W. Utomo, A. L. Kocen, S. Jin, Y. Deng, V. X. Zhu, S. Moganty, G. W. Coates, L. A. Archer, *Angew Chem., Int. Ed.* **2022**, *61*, 202116214.

[8] L. Gan, R. Chen, X. Xu, M. Zan, Q. Li, Q. Wang, X. Yu, H. Li, *J. Power Sources* **2022**, *551*, 232182.

[9] a) Z. Piao, R. Gao, Y. Liu, G. Zhou, H. M. Cheng, *Adv. Mater.* **2023**, *35*, 2206009; b) M. Yeddala, L. Rynearson, B. L. Lucht, *ACS Energy Lett.* **2023**, *8*, 4782; c) X. Yi, X. Li, J. Zhong, S. Wang, Z. Wang, H. Guo, J. Wang, G. Yan, *Adv. Funct. Mater.* **2022**, *32*, 2209523;

[10] a) G.-X. Li, H. Jiang, R. Kou, D. Wang, A. Nguyen, M. Liao, P. Shi, A. Silver, D. Wang, *ACS Energy Lett.* **2022**, *7*, 2282; b) Q. Li, Z. Cao, W. Wahyudi, G. Liu, G.-T. Park, L. Cavallo, T. D. Anthopoulos, L. Wang, Y.-K. Sun, H. N. Alshareef, J. Ming, *ACS Energy Lett.* **2020**, *6*, 69.

[11] a) J.-S. Shin, C.-H. Han, U.-H. Jung, S.-I. Lee, H.-J. Kim, K. Kim, *J. Power Sources* **2002**, *109*, 47; b) Y. Guo, S. Pan, X. Yi, S. Chi, X. Yin, C. Geng, Q. Yin, Q. Zhan, Z. Zhao, F. M. Jin, H. Fang, Y. B. He, F. Kang, S. Wu, Q. H. Yang, *Adv. Mater.* **2024**, *36*, 2308493; c) S. B. Lu Li, Y. Wang, Z. Chen, P. Hundekar, B. Wang, J. Shi, Y. Shi, S. Narayanan, N. Koratkar, *Science* **2018**, *359*, 1513; d) Y. Zhu, Y. Chen, J. Chen, J. Yin, Z. Sun, G. Zeng, X. Wu, L. Chen, X. Yu, H. Luo, Y. Yan, H. Zhang, B. Zhang, X. Kuai, Y. Tang, J. Xu, W. Yin, Y. Qiu, Q. Zhang, Y. Qiao, S. G. Sun, *Adv. Mater.* **2024**, *36*, 2312159.

[12] a) Y. Xue, Y. Wang, H. Zhang, W. Kong, Y. Zhou, B. Kang, Z. Huang, H. Xiang, *Angew Chem., Int. Ed.* **2025**, *64*, 202414201; b) X. Cao, L. Zou, B. E. Matthews, L. Zhang, X. He, X. Ren, M. H. Engelhard, S. D. Burton, P. Z. El-Khoury, H.-S. Lim, C. Niu, H. Lee, C. Wang, B. W. Arey, C. Wang, J. Xiao, J. Liu, W. Xu, J.-G. Zhang, *Energy Stor. Mater.* **2021**, *34*, 76; c) H. Cheng, Q. Sun, L. Li, Y. Zou, Y. Wang, T. Cai, F. Zhao, G. Liu, Z. Ma, W. Wahyudi, Q. Li, J. Ming, *ACS Energy Lett.* **2022**, *7*, 490.

[13] a) S. Fang, Y. Zhang, X. Liu, *Chem. Eng. J.* **2021**, *426*, 131880; b) T. T. Hagos, B. Thirumalraj, C. J. Huang, L. H. Abrha, T. M. Hagos, G. B. Berhe, H. K. Bezabh, J. Cherng, S. F. Chiu, W. N. Su, B. J. Hwang, *ACS Appl. Mater. Interfaces* **2019**, *11*, 9955; c) Y. Jin, N. H. Kneusels, L. E. Marbella, E. Castillo-Martinez, P. Magusin, R. S. Weatherup, E. Jonsson, T. Liu, S. Paul, C. P. Grey, *J. Am. Chem. Soc.* **2018**, *140*, 9854; d) Y. Yang, J. Xiong, S. Lai, R. Zhou, M. Zhao, H. Geng, Y. Zhang, Y. Fang, C. Li, J. Zhao, *ACS Appl. Mater. Interfaces* **2019**, *11*, 6118; e) S. Tan, Y. Jiang, S. Ni, H. Wang, F. Xiong, L. Cui, X. Pan, C. Tang, Y. Rong, Q. An, L. Mai, *Natl. Sci. Rev.* **2022**, *9*, nwac183.

[14] a) B. Han, Z. Zhang, Y. Zou, K. Xu, G. Xu, H. Wang, H. Meng, Y. Deng, J. Li, M. Gu, *Adv. Mater.* **2021**, *33*, 2100404; b) G. Li, X. Duan, X. Liu, R. Zhan, X. Wang, J. Du, Z. Chen, Y. Li, Z. Cai, Y. Shen, Y. Sun, *Adv. Mater.* **2023**, *35*, 2207310.

[15] a) Y. Zhang, S. Du, Y. Pang, X. Gao, D. Luo, X. Xiang, *J. Alloys Compd.* **2022**, *895*, 162646; b) Z. Fan, X. Chen, J. Shi, H. Nie, X. Zhang, X. Zhou, X. Xie, Z. Xue, *Nano-Micro Lett.* **2025**, *17*, 128.

[16] a) J. M. Larson, H. A. Bechtel, R. Kostecki, *Adv. Funct. Mater.* **2024**, *34*, 2406643; b) G. Weber, E. Sciora, J. Guichard, F. Bouyer, I. Bezverkhyy, J. M. Salazar, C. Dirand, F. Bernard, H. Lecoq, R. Besnard, J.-P. Bellat, *J. Therm. Anal. Calorim.* **2018**, *132*, 1055.

[17] H. Ota, Y. Sakata, A. Inoue, S. Yamaguchi, *J. Electrochem. Soc.* **2004**, *151*, A1659.

[18] a) J. Zhang, X. Yue, Z. Wu, Y. Chen, Y. Bai, K. Sun, Z. Wang, Z. Liang, *Nano Lett.* **2023**, *23*, 9609; b) X. Chen, R. Zhang, R. Zhao, X. Qi, K. Li, Q. Sun, M. Ma, L. Qie, Y. Huang, *Energy Stor. Mater.* **2020**, *31*, 181; c) X. Cao, X. Ren, L. Zou, M. H. Engelhard, W. Huang, H. Wang, B. E. Matthews, H. Lee, C. Niu, B. W. Arey, Y. Cui, C. Wang, J. Xiao, J. Liu, W. Xu, J.-G. Zhang, *Nat. Energy* **2019**, *4*, 796; d) C. Deng, B. Yang, Y. Liang, Y. Zhao, B. Gui, C. Hou, Y. Shang, J. Zhang, T. Song, X. Gong, N. Chen, F. Wu, R. Chen, *Angew. Chem., Int. Ed.* **2024**, *63*, 202400619; e) L. Yu, S. Chen, H. Lee, L. Zhang, M. H. Engelhard, Q. Li, S. Jiao, J. Liu, W. Xu, J.-G. Zhang, *ACS Energy Lett.* **2018**, *3*, 2059; f) F. Zhang, P. Zhang, W. Zhang, P. R. Gonzalez, D. Q. Tan, Y. Ein-Eli, *Adv. Mater.* **2024**, *36*, 2410277; g) J. Jiang, M. Li, X. Liu, J. Yi, Y. Jiang, C. Wu, H. Liu, B. Zhao, W. Li, X. Sun, J. Zhang, S. Dou, *Adv. Energy Mater.* **2024**, *14*, 2400365; h) S. Ha, S.-J. Bae, C. Lim, C. G. Min, S. Myeong, W.-J. Song, Y.-S. Lee, *J. Ind. Eng. Chem.* **2024**, *146*, 757; i) Y. Wen, J. Ding, Y. Yang, X. Lan, J. Liu, R. Hu, M. Zhu, *Adv. Funct. Mater.* **2021**, *32*, 2109377; j) A. R. Jeon, B. Y. Han, M. Kwon, S. H. Yu, K. Y. Chung, J. Shim, M. Lee, *Small* **2024**, *20*, 2402213.

[19] a) Q. Liu, D. Zhou, D. Shanmukaraj, P. Li, F. Kang, B. Li, M. Armand, G. Wang, *ACS Energy Lett.* **2020**, *5*, 1456; b) N. Yang, Y. Cui, H. Su, J. Peng, Y. Shi, J. Niu, F. Wang, *Angew. Chem., Int. Ed. Engl.* **2023**, *62*, 202304339; c) P. Jaumaux, Q. Liu, D. Zhou, X. Xu, T. Wang, Y. Wang, F. Kang, B. Li, G. Wang, *Angew. Chem., Int. Ed.* **2020**, *59*, 9134.

[20] K. Wu, A. Li, J. Tan, F. Zhou, H. Yan, P. Wang, T. Xie, Q. Zeng, C. Han, Q. Liu, B. Li, *Angew. Chem., Int. Ed.* **2024**, *63*, 202410347.